

Dynamic analysis of a novel multilink-spring mechanism for vibration isolation and energy harvesting

Jia-Heng Xie(谢佳衡), Tao Yang(杨涛), and Jie Tang(唐介)

Citation: Chin. Phys. B, 2024, 33 (**5**): 050706. DOI: 10.1088/1674-1056/ad21f6
Journal homepage: http://cpb.iphy.ac.cn; http://iopscience.iop.org/cpb

What follows is a list of articles you may be interested in

Inertial focusing and rotating characteristics of elliptical and rectangular particle pairs in channel flow

Pei-Feng Lin(林培锋), Xiao Hu(胡箫), and Jian-Zhong Lin(林建忠)
Chin. Phys. B, 2022, 31 (**8**): 080501. DOI: 10.1088/1674-1056/ac5983

ffect of plasma on combustion characteristics of boron

Peng Zhang(张鹏), Wenli Zhong(钟文丽), Qian Li(李倩), Bo Yang(杨波), Zhongguang Li(李忠光), Xiao Luan(栾骁)
Chin. Phys. B, 2017, 26 (**11**): 110501. DOI: 10.1088/1674-1056/26/11/110501

Modified Chapman-Enskog expansion: A new way to treat divergent series

Zhen-Su She(佘振苏)
Chin. Phys. B, 2017, 26 (**8**): 080501. DOI: 10.1088/1674-1056/26/8/080501

A multiple-relaxation-time lattice Boltzmann method for high-speed compressible flows

Li Kai (李凯), Zhong Cheng-Wen (钟诚文)
Chin. Phys. B, 2015, 24 (**5**): 050501. DOI: 10.1088/1674-1056/24/5/050501

A statistical model for predicting thermal chemical reaction rate

Lin Zheng-Zhe (林正喆), Li Wang-Yao (李王尧), Ning Xi-Jing (宁西京)
Chin. Phys. B, 2014, 23 (**5**): 050501. DOI: 10.1088/1674-1056/23/5/050501

Multi-rate sensor fusion-based adaptive discrete finite-time synergetic control for flexible-joint mechanical systems

Xue Guang-Yue (薛广月), Ren Xue-Mei (任雪梅), Xia Yuan-Qing (夏元清)
Chin. Phys. B, 2013, 22 (**10**): 100702. DOI: 10.1088/1674-1056/22/10/100702

Dynamic analysis of a novel multilink-spring mechanism for vibration isolation and energy harvesting

Jia-Heng Xie(谢佳衡)[1], Tao Yang(杨涛)[2,†], and Jie Tang(唐介)[3]

[1] *Research & Development Institute of Northwestern Polytechnical University in Shenzhen, Shenzhen* 518057, *China*
[2] *Department of Engineering Mechanics, Northwest Polytechnical University, Xi'an* 710072, *China*
[3] *Applied Mechanics and Structure Safety Key Laboratory of Sichuan Province, School of Mechanics and Aerospace, Southwest Jiaotong University, Chengdu* 610031, *China*

(Received 8 December 2023; revised manuscript received 19 January 2024; accepted manuscript online 24 January 2024)

Due to technical limitations, existing vibration isolation and energy harvesting (VIEH) devices have poor performance at low frequency. This paper proposes a new multilink-spring mechanism (MLSM) that can be used to solve this problem. The VIEH performance of the MLSM under harmonic excitation and Gaussian white noise was analyzed. It was found that the MLSM has good vibration isolation performance for low-frequency isolation and the frequency band can be widened by adjusting parameters to achieve a higher energy harvesting power. By comparison with two special cases, the results show that the MLSM is basically the same as the other two oscillators in terms of vibration isolation but has better energy harvesting performance under multistable characteristics. The MLSM is expected to reduce the impact of vibration on high-precision sensitive equipment in some special sites such as subways and mines, and at the same time supply power to structural health monitoring devices.

Keywords: multilink-spring mechanism, nonlinear dynamics, vibration isolation, energy harvester

PACS: 07.10.–h, 05.20.Dd, 07.10.Fq, 45.20.dH **DOI:** 10.1088/1674-1056/ad21f6

1. Introduction

Vibration often has a negative impact on engineering structures and is inevitable, so vibration control is a hot and difficult topic in structural safety. Fortunately, the application of nonlinear theory in vibration isolation in recent years can solve this problem effectively;[1–3] quasi-zero stiffness (QZS) theory is one such theory. A vibration isolator with QZS characteristics can achieve arbitrarily small stiffness while at the same time having an excellent supporting capacity. Such isolators have been widely used in engineering design.[4]

Many interesting vibration isolators have been designed according to QZS characteristics. For example, Liu *et al.* proposed[5] a vibration isolator with a six degree-of-freedom mechanism, and found the performance to be much better than that of a linear isolator by comparative analysis of force transmissibility. Yoshikazu *et al.*[6] used cranks and a screw jack to achieve QZS characteristics under different loading masses. Yuan *et al.*[7] found a way to achieve negative stiffness using electromagnets and connected them in parallel with wire springs to achieve QZS characteristics; this had a compact structure. Georgios *et al.*[8] designed a novel QZS vibration isolator using a gas spring and demonstrated the stability and feasibility of this device to be better than that of the linear one. By combining rods with springs, Zhang *et al.*[9] and Sun and Jing[10] designed vibration isolators with a scissor-type structure. Yang *et al.*[11] and Yan *et al.*[12] achieved QZS characteristics by using rigid links and springs. At the same time, an SD oscillator based on dipteran flight[13] was proposed for the design of new vibration isolators.[14] Yu *et al.*[15] used a torsion bar spring to achieve QZS characteristics and verified the validity of the proposed model using finite-element method simulation. Vibration isolators with QZS characteristics have a wider isolation bandwidth and a smaller force transmissibility than linear ones.[16] However, the problem of a large resonance peak of the isolators with QZS characteristics needs to be solved urgently.

Vibration energy can also be harvested. Vibration energy from wind,[17] ocean waves,[18] human motion[19] and mechanical structures[20,21] can be converted into electrical energy. Because battery life is short, maintenance costs are high and waste batteries are harmful to the environment, vibration energy harvesting has become a hot research field. In some closed situations, such as subways and mines, vibration energy harvesting is the best choice, and can also avoid some catastrophic accidents. Present methods of vibration energy harvesting are magnetoelectric,[22–24] piezoelectric,[25–27] magnetostrictive[28–30] and triboelectric nanogenerators.[31–33] In recent years, to overcome the problem of the narrow effective bandwidth of linear vibration energy harvesting, researchers have applied nonlinear structures to the field of vibration energy harvesting.[34–36] The application of nonlinear structure can increase the number of potential wells to achieve bistable,[37,38] tristable[39,40] and multistable characteristics.[41,42] These energy harvesters can

[†]Corresponding author. E-mail: yangtscn@nwpu.edu.cn

© 2024 Chinese Physical Society and IOP Publishing Ltd

move across potential wells at different equilibrium positions, thereby widening the frequency band. These harvesters have a higher output power under the same external excitation than conventional ones.[43]

The effective combination and application of vibration isolation and energy harvesting (VIEH) has also been further developed.[44,45] Lu *et al.*[46] proposed a Stewart platform for VIEH in parallel with a leaf spring and analyzed its VIEH performance using the harmonic balance method. Zou *et al.*[47] proposed an energy harvester with an integrated vibration isolator, which can achieve tristable characteristics through structural design. Liu *et al.*[48] used the method of combining a buckled beam with the spring to design a QZS device capable of VIEH; this has a better energy harvesting performance than a cantilever beam. Zang *et al.*[49] proposed a vibrational energy harvesting isolator which uses levers to achieve nonlinear characteristics. The energy harvesting powers of current VIEH oscillators are generally low.[50] To solve this problem, it is necessary to increase the wideband to improve the efficiency of energy harvesting performance.

Therefore, this paper proposes a new multilink-spring mechanism (MLSM) to meet the needs of low-frequency (below 20 Hz) VIEH by applying different parameters. By adjusting the parameters, the oscillator can achieve QZS and multistable characteristics. The organization of this article is as follows: in Section 2, Newton's and Kirchhoff's laws are used to build the mathematical model; in Section 3, the extended averaging method is used to analyze the VIEH performance of the MLSM; in Section 4, the Fokker–Planck–Kolmogorov equation[51] is used to analyze the energy harvesting performance of the MLSM under Gaussian white noise as a random excitation condition; in Section 5, the MLSM is compared with the two cases based on QZS characteristics; Section 6 gives our conclusions.

2. Generic model and modeling

2.1. Device description

Figure 1(a) illustrates the structure of the MLSM. First, the vertical springs I and the vertical rails support the load-bearing table with mass m mounted on the main frame and the magnet is fixed on the vertical rails. The load-bearing table, magnet and the vertical rails can only move in the vertical direction. Second, vertical springs Ⅱ are mounted at the bottom of the main frame; the horizontal distance between vertical springs I and Ⅱ is adjustable. Third, the horizontal rails are mounted on the side walls of the main frame and can only be moved in a vertical direction. Next, the horizontal springs and the sliders are mounted on the horizontal rails, and the sliders move with the movement of the horizontal springs. Finally, the rigid links I are hinged on vertical springs Ⅱ at one end and to the sliders at the other end. The rigid links Ⅱ hang at one end to the sliders and at the other end to the load-bearing table. The magnet and the coil form the electromechanical transduction system (EMT).

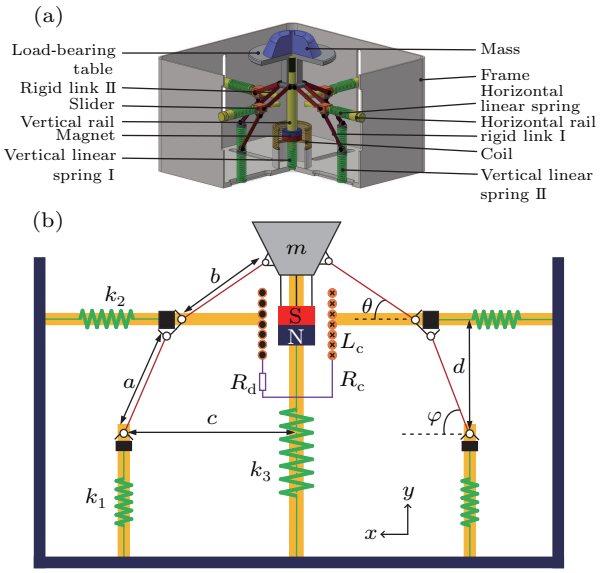


Fig. 1. Model design of the MLSM: (a) 3D structure, (b) simplified structure.

Since the MLSM is a symmetrical structure, it can be simplified to a 2D structure, as shown in Fig. 1(b). Here k_1, k_2, and k_3 are the stiffness of vertical springs Ⅱ, horizontal springs and vertical springs I, respectively. Vertical springs I and vertical springs Ⅱ are compressed, and the horizontal springs are in a tense state. a and b are the length of rigid links I and rigid links Ⅱ, c is the horizontal distance between vertical springs I and vertical springs Ⅱ and d is the distance from the horizontal rails to the tip of vertical springs Ⅱ. φ is the angle between rigid links I and the horizontal direction, while θ is the angle between rigid links I and the horizontal direction. B_e is the strength of the magnetic induction, L_c is the length of the coil and I_R is the current intensity. When the load-bearing table moves in the horizontal direction, it will entangle the magnet to move with it. Therefore, the magnetic flux in the coil changes when magnet moves, and the MLSM converts vibrational energy into electrical energy.

2.2. Geometric relation and modeling

As shown in Fig. 1, when the load-bearing table is forced to move in the y direction, the restoring force $F(y)$ produced by springs in the y direction can be obtained by Newton's law

$$F(y) = -2k_1\Delta l\tan\varphi\tan\theta - 2k_2\Delta x\tan\theta + k_3\Delta y, \tag{1}$$

where Δy is the displacement of the load-bearing table, Δx is the displacement of sliders in the x direction and Δl is the shape variable of vertical springs Ⅱ, which is written as

$$\Delta l = \sqrt{a^2 - \Delta x^2} - d. \tag{2}$$

The geometrical relationship between x and y is

$$(c-x)^2+y^2=b^2, \tag{3}$$

where

$$x=\Delta x,\ \ y=\sqrt{b^2-c^2}+\Delta y.$$

Depending on the geometrical relationship, φ and θ can be expressed as

$$\begin{cases}\tan\varphi=\dfrac{x}{\sqrt{a^2-x^2}},\\ \tan\theta=\dfrac{y}{c-x}.\end{cases} \tag{4}$$

Therefore, the restoring force is written as

$$\begin{aligned}F(y)\ =\ &-2k_1y\left(-1+\frac{c}{\sqrt{b^2-y^2}}\right)\\ &\times\left(1-\frac{d}{\sqrt{a^2-\left(c-\sqrt{b^2-y^2}\right)^2}}\right)\\ &-2k_2y\left(1-\frac{c}{\sqrt{b^2-y^2}}\right)+k_3\left(y-\sqrt{b^2-c^2}\right).\end{aligned} \tag{5}$$

When the EMT is considered, the dynamical equation of the MLSM can be deduced as

$$m\ddot{Y}+F(y)+mg+C_e\dot{y}+B_eL_cI_R=0, \tag{6}$$

where Y is the absolute displacement of the MLSM and $Y=y+\hat{y}$. Let $mg=k_3\sqrt{b^2-c^2}$. Equations (6) can then be rewritten as

$$\begin{aligned}&m\ddot{Y}-2k_1y\left(-1+\frac{c}{\sqrt{b^2-y^2}}\right)\\ &\times\left(1-\frac{d}{\sqrt{a^2-\left(c-\sqrt{b^2-y^2}\right)^2}}\right)\\ &-2k_2y\left(1-\frac{c}{\sqrt{b^2-y^2}}\right)+k_3y+C\dot{y}+B_eL_cI_R=0.\end{aligned} \tag{7}$$

According to Kirchhoff's law

$$\dot{I}_R(t)L_i+(R_d+R_c)I_R-B_eL_c\dot{y}(t)=0, \tag{8}$$

where L_i is the inductance of the coil, R_c is the resistance of the coil and R_d is the variable of the load resistance in the electrical circuit.

Neglecting the mass of other components, the kinetic energy $T(Y)$ and the potential energy $U(y)$ of the MLSM can be written as

$$T(Y)=\frac{1}{2}m\dot{Y}^2, \tag{9}$$

$$\begin{aligned}U(y)=2k_1&\left(\frac{1}{2}y^2+c\sqrt{b^2-y^2}\right.\\ &\left.-d\sqrt{a^2-\left(c-\sqrt{b^2-y^2}\right)^2}\right)+k_2\left(c-\sqrt{b^2-y^2}\right)^2\\ &+\frac{k_3y^2}{2}-k_3\sqrt{b^2-c^2}y+mgy.\end{aligned} \tag{10}$$

Equations (7) and (8) can be deduced as

$$\begin{cases}\ddot{y}+\xi\dot{y}+P(y)+\eta I_R=-\ddot{\hat{y}},\\ \dot{I}_R(t)+\lambda I_R-\gamma\dot{y}(t)=0,\end{cases} \tag{11}$$

where $P(y)$ is the dimensionless restoring force, which can be written as

$$\begin{aligned}P(y)=&-y\left(-1+\frac{c}{\sqrt{b^2-y^2}}\right)\\ &\times\left(1-\frac{d}{\sqrt{a^2-\left(c-\sqrt{b^2-y^2}\right)^2}}\right)\\ &-\alpha y\left(1-\frac{c}{\sqrt{b^2-y^2}}\right)+\beta y,\end{aligned} \tag{12}$$

$$\begin{aligned}&y(t)=y(\omega_1,T),\ \ \dot{y}(t)=\omega_1y(t),\ \ \ddot{y}(t)=\omega_1^2y(t),\\ &\xi=\frac{C_e}{m\omega_1},\ \ \omega_1^2=\frac{2k_1}{m},\ \ \omega_2^2=\frac{2k_2}{m},\ \ \omega_3^2=\frac{k_3}{m},\\ &\alpha=\frac{\omega_2^2}{\omega_1^2},\ \ \beta=\frac{\omega_3^2}{\omega_1^2},\ \ \eta=\frac{BeLc}{m\omega_1^2},\ \ \gamma=\frac{BeLc}{L_i},\\ &\lambda=\frac{R_d+R_c}{L_i}.\end{aligned} \tag{13}$$

The Hamiltonian function of the MLSM can be deduced as

$$\begin{aligned}&\frac{1}{2}\dot{y}^2+\left(\frac{1}{2}y^2+c\sqrt{b}^2-y^2-d\sqrt{a^2-\left(c-\sqrt{b^2-y^2}\right)^2}\right)\\ &+\frac{\alpha}{2}\left(c-\sqrt{b^2-y^2}\right)^2+\frac{\beta}{2}y^2-cb+d\sqrt{a^2-(c-b)^2}\\ &-\frac{\alpha}{2}(c-b)^2=H_0.\end{aligned} \tag{14}$$

The parameters are shown in Table 1.

Table 1. Parameters for the MLSM.

Symbol	Definition
a,b,c,d	geometric coefficients
$\hat{y}$	environmental base excitation
ξ	linear damping coefficient
η	electromechanical coupling coefficient
γ	electromagnetic coupling coefficient
α,β	natural frequency ratio

Figure 2 describes the phase diagram with different values of H_0 by adjusting different parameters a, b, c, d, α, and, β, which can obtain the relationship of the displacement and the

velocity of the MLSM. Figures 2(a)–2(d) describe the mono-, bi-, tri- and quad-stable potential wells of the MLSM, respectively. It is obvious from Figs. 2(b) and 2(d) that when H_0 is low, which corresponds to the green line, the MLSM cannot achieve interwell oscillation.

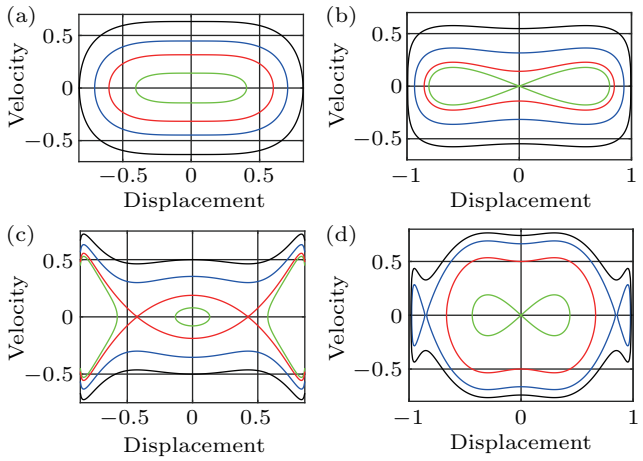


Fig. 2. The phase diagrams of the MLSM with different geometric coefficients and natural frequency ratios: (a) $a=\sqrt{2}/2$, $b=1$, $c=1/2$, $d=1/2$, $\alpha=4$, $\beta=2$, (b) $a=1$, $b=1$, $c=1/2$, $d=1$, $\alpha=1$, $\beta=2/5$, (c) $a=1/2$, $b=1$, $c=1$, $d=1/5$, $\alpha=1/50$, $\beta=3/50$, (d) $a=3/5$, $b=1$, $c=3/5$, $d=1/2$, $\alpha=1/50$, $\beta=1/50$.

2.3. Characteristic of the QZS system

We expand the dimensionless restoring force $P(y)$ by using Taylor's theorem

$$P(y)=\Omega_1 y+\Omega_2 y^3+\Omega_3 y^5+\Omega_4 y^7+O[y]^8, \tag{15}$$

where

$$\Omega_1=\left(\left(\frac{c}{b}-1\right)J_1+\alpha\left(\frac{c}{b}-1\right)+\beta\right),$$

$$\Omega_2=\frac{\left(cJ_1+\frac{b(c-b)}{c}J_2+c\alpha\right)}{2b^3},$$

$$\Omega_3=\frac{\left(\frac{3cJ_1}{b}+2J_2+(c-b)J_3+\frac{3c\alpha}{b}\right)}{8b^4},$$

$$\Omega_4=\frac{\left(9J_2+3cJ_3+3(b-c)(J_4+J_5)+\frac{15cJ_1}{b}+\frac{15c\alpha}{b}\right)}{48b^6},$$

$$J_1=\left(\frac{d}{\sqrt{a^2-(b-c)^2}}-1\right),$$

$$J_2=-\frac{(b-c)cd}{\left(a^2-(b-c)^2\right)^{3/2}},$$

$$J_3=\frac{\left(3b^3+a^2c-7b^2c+5bc^2-c^3\right)d}{\left(a^2-(b-c^2)\right)^{5/2}},$$

$$J_4=\frac{\left(5b^5-19b^4c+28b^3c^2+5b^2c\left(a^2-4c^2\right)\right)d}{\left(a^2-(b-c)^2\right)^{7/2}},$$

$$J_5=\frac{\left(c^2-a^2\right)\left(7bc^2+c\left(a^2-c^2\right)\right)d}{\left(a^2-(b-c)^2\right)^{7/2}}.$$

Because the displacement near the equilibrium position is small, the dimensionless stiffness $P'(y)$ can be expressed as the derivative of $P(y)$ for y

$$\begin{aligned}P'(y)=&\frac{dy^2\left(c-\sqrt{b^2-y^2}\right)^2}{(b^2-y^2)\left(a^2-\left(c-\sqrt{b^2-y^2}\right)^2\right)^{3/2}}\\&-\frac{cy^2\left(1-\dfrac{d}{\sqrt{a^2-\left(c-\sqrt{b^2-y^2}\right)^2}}\right)}{(b^2-y^2)^{3/2}}\\&+\left(\frac{c}{\sqrt{b^2-y^2}}-1\right)\left(\frac{d}{\sqrt{a^2-\left(c-\sqrt{b^2-y^2}\right)^2}}-1\right)\\&+\frac{\alpha cy^2}{(b^2-y^2)^{3/2}}+\alpha\left(\frac{c}{\sqrt{b^2-y^2}}-1\right)+\beta.\end{aligned} \tag{16}$$

If the MLSM is in the equilibrium position ($y=0$), QZS characteristics can be achieved by adjusting the parameters. Therefore, the QZS characteristics of the MLSM can be obtained as

$$(B-1)\left(\frac{C}{\sqrt{A^2-(1-B)^2}}-1+\alpha\right)+\beta=0, \tag{17}$$

where $A=a/b$, $B=c/b$, $C=d/b$.

Let $a=\sqrt{2}/2$, $b=1$, $c=1/2$, $d=1/2$, $\alpha=4$, and $\beta=2$; the dimensionless restoring force $P(y)$ after expansion by Taylor theorem is

$$P(y)=\frac{3y^3}{2}-\frac{3y^5}{8}+\frac{39y^7}{16}\cdots. \tag{18}$$

Therefore, the system has QZS characteristics.

Figure 3 shows the influence of different geometric coefficients and natural frequency ratios on dimensionless restoring force–displacement and stiffness–displacement curves. The geometric coefficients and natural frequency ratio of the MLSM are as follows: (a) and (e) $a=\sqrt{2}/2$, $b=1$, $c=1/2$, $d=1/2$, $\alpha=4$, $\beta=2$; (b) and (f) $a=1$, $b=1$, $c=1/2$, $d=1$, $\alpha=1$, $\beta=2/5$; (c) and (g) $a=1/2$, $b=1$, $c=1$, $d=1/5$, $\alpha=1/50$, $\beta=3/50$; (d) and (h) $a=3/5$, $b=1$, $c=3/5$, $d=1/2$, $\alpha=1/50$, $\beta=1/50$. As shown in Figs. 3(a)–3(d), the dimensionless restoring force has one, three, five and seven equilibrium points. This means that the MLSM can achieve mono-, bi-, tri- and quad-stable potential wells, respectively, as shown in Fig. 2. In Figs. 3(a) and 3(e), when $y=0$ the dimensionless restoring force $P(y)=0$ and the dimensionless stiffness $P'(y)=0$; this means that the MLSM has QZS

characteristics. As shown in Figs. 3(f)–3(h), the dimensionless stiffness of the MLSM has a negative stiffness characteristic, which should be avoided in engineering applications.

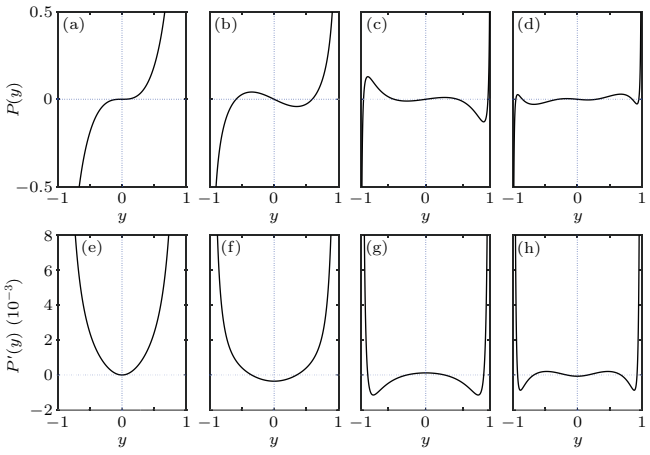


Fig. 3. The dimensionless restoring force $P(y)$ and stiffness $P'(y)$ of the MLSM with different geometric coefficients and natural frequency ratios.

Figure 4 describes the effect of parameters a, b, c, and d on the dimensionless system stiffness $P'(y)$, where the geometric coefficients of the MLSM are (a) and (b) $c = 1/2$, $d = 1/2$ and (c) and (d) $a = \sqrt{2}/2$, $b = 1$. It can be seen from Fig. 4(a) that when the parameter a increases, the stiffness of the equilibrium position ($y = 0$) increases gradually, when $a < \sqrt{2}/2$, $P'(y) < 0$, when $a > \sqrt{2}/2$, $P'(y) > 0$. As shown in Fig. 4(b), the stiffness $P'(y)$ of the equilibrium position decreases gradually when parameter b increases: $P'(y) > 0$ when $b < 1$ and $P'(y) < 0$ when $b > 1$. In Fig. 4(c) the stiffness $P'(y)$ of the equilibrium position gradually increases when the parameter c increases: $P'(y) < 0$ when $c < 1/2$, $P'(y) > 0$ when $c > 1/2$. It can be seen from Fig. 4(d) that when parameter d increases, the stiffness $P'(y)$ of the equilibrium positiongradually decreases: when $d < 1$, $P'(y) > 0$ and when $d > 1$, $P'(y) < 0$.

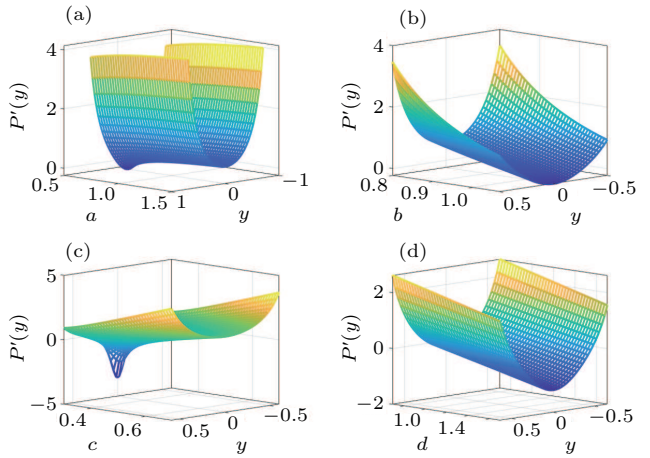


Fig. 4. Stiffness surfaces of the MLSM with different geometric coefficients a, b, c, and d.

2.4. Model decoupling

The solution of Eq. (11) can be obtained as

$$\begin{cases} y(t) = A_{\mathrm{em}}(t)\cos\phi(t), \\ \dot{y}(t) = -\omega(A_{\mathrm{em}},\phi)A_{\mathrm{em}}(t)\sin\phi(t), \\ \phi(t) = \Phi(t) + \Psi(t), \\ \omega(A_{\mathrm{em}},\phi) = \dfrac{\mathrm{d}\Phi(t)}{\mathrm{d}t}, \\ I_{\mathrm{R}}(t) = I_{\mathrm{R0}}\mathrm{e}^{-\lambda t} + \int_0^t \mathrm{e}^{-\lambda t}\dot{y}(t-t_{\mathrm{s}})\,\mathrm{d}t_{\mathrm{s}}. \end{cases} \tag{19}$$

Because $I_{\mathrm{R0}}\mathrm{e}^{-\lambda t}$ decays rapidly after external excitation is produced, the effect on the steady-state response can be negligible. $\dot{y}(t-t_{\mathrm{s}})$ can be written as

$$\begin{aligned} &\dot{y}(t-t_{\mathrm{s}}) \\ &= -\omega(A_{\mathrm{em}},\phi)A_{\mathrm{em}}(t)\sin[\omega(A_{\mathrm{em}},\phi)(t-t_{\mathrm{s}}) + \Psi(t)] \\ &= y(t)\,\omega(A_{\mathrm{em}},\phi)\sin[\omega(A_{\mathrm{em}},\phi)t_{\mathrm{s}}] \\ &\quad + \dot{y}(t)\cos[\omega(A_{\mathrm{em}},\phi)t_{\mathrm{s}}]. \end{aligned} \tag{20}$$

Thus, with the inward formula (19) and eliminating the index decay term, the output current $I_{\mathrm{R}}(t)$ is given by

$$\begin{aligned} I_{\mathrm{R}}(t) &= \frac{A_{\mathrm{em}}(t)\gamma\omega(A_{\mathrm{em}},\phi)}{\lambda^2+\omega^2(A_{\mathrm{em}},\phi)} \\ &\quad \times[\omega(A_{\mathrm{em}},\phi)\cos\phi(t) - \lambda\sin\phi(t)] \\ &= \frac{\gamma}{\lambda^2+\omega^2(A_{\mathrm{em}},\phi)}\left[\omega^2(A_{\mathrm{em}},\phi)y + \lambda\dot{y}\right]. \end{aligned} \tag{21}$$

Equation (11) can be deduced after model decoupling

$$\ddot{y} + (\xi + V_{\mathrm{em}})\dot{y} + W_{\mathrm{em}}y + P(y) = -\hat{\ddot{y}}, \tag{22}$$

where $V_{\mathrm{em}} = (\eta\gamma\lambda)/\left(\lambda^2+\omega^2(A_{\mathrm{em}},\phi)\right)$ and $W_{\mathrm{em}} = [\eta\gamma\omega^2(A_{\mathrm{em}},\phi)]/\lambda^2+\omega^2(A_{\mathrm{em}},\phi)$.

Thus, equation (22) can be rewritten as

$$\begin{cases} \dfrac{\mathrm{d}y}{\mathrm{d}t} = v, \\ \dfrac{\mathrm{d}v}{\mathrm{d}t} = -(\xi + V_{\mathrm{em}})v - P_{\mathrm{E}}(y) - \hat{\ddot{y}}, \end{cases} \tag{23}$$

where $P_{\mathrm{E}}(y)$ is the restoring force when considering the influence of the electromotive force, which can be expressed as

$$P_{\mathrm{E}}(y) = W_{\mathrm{em}}y + P(y). \tag{24}$$

3. Dynamical analysis of harmonic excitation

To analyze the effect of harmonic excitation on the MLSM, this section analyzes the amplitude–frequency response, the force transmissibility and the energy harvesting performance under harmonic excitation.

3.1. Amplitude–frequency analysis of a QZS system

In this subsection, the external excitation is harmonic excitation, $\hat{y} = f\cos(\omega t)$, where f and ω correspond to the amplitude and the frequency of the excitation, respectively. Equation (24) can be written as

$$\ddot{y} + (\xi + V_{\mathrm{em}})\dot{y} + P_{\mathrm{E}}(y) = f\cos(\omega t), \quad |y| < b. \tag{25}$$

The amplitude–frequency response of the MLSM is analyzed using the extended averaging method. The dimensionless restoring force $P(y)$ can be expanded by the Taylor theorem

$$P_{\mathrm{E}}(y) = (W_{\mathrm{em}} + \Omega_1) y + \Omega_2 y^3 + \Omega_3 y^5 + \Omega_4 y^7. \tag{26}$$

Therefore, equation (23) can be expressed as

$$\begin{aligned} &\ddot{y} + (\xi + V_{\mathrm{em}}) + (W_{\mathrm{em}} + \Omega_1) y + \Omega_2 y^3 + \Omega_3 y^5 + \Omega_4 y^7 \\ &= f\cos(\omega t), \quad |y| < b. \end{aligned} \tag{27}$$

By using the extended averaging method, the solution of Eq. (27) can be deduced as

$$\begin{cases} \dfrac{\mathrm{d}A_{\mathrm{em}}}{\mathrm{d}t} = -\dfrac{1}{\omega}\Gamma(A_{\mathrm{em}}, \Psi)\sin(\omega t + \Psi), \\ \dfrac{\mathrm{d}\Psi}{\mathrm{d}t} = -\dfrac{1}{A_{\mathrm{em}}\omega}\Gamma(A_{\mathrm{em}}, \Psi)\cos(\omega t + \Psi), \end{cases} \tag{28}$$

where

$$\begin{aligned} &\Gamma(A_{\mathrm{em}}, \Psi) \\ &= A_{\mathrm{em}}\omega^2\cos\phi + (\xi + V_{\mathrm{em}})(\omega A_{\mathrm{em}}\sin\phi) \\ &\quad - (W_{\mathrm{em}} + \Omega_1)(A_{\mathrm{em}}\cos\phi) - \Omega_2(A_{\mathrm{em}}\cos\phi)^3 \\ &\quad - \Omega_3(A_{\mathrm{em}}\cos\phi)^5 - \Omega_4(A_{\mathrm{em}}\cos\phi)^7 + f\cos(\omega t) \end{aligned} \tag{29}$$

and $\phi(t) = \omega t + \Psi$.

Integral ϕ is in the range $[0, 2\pi]$ and takes the average, which is given by

$$\begin{cases} \dfrac{\mathrm{d}A_{\mathrm{em}}}{\mathrm{d}t} = \dfrac{1}{2\pi}\displaystyle\int_0^{2\pi} -\frac{1}{\omega}\Gamma(A_{\mathrm{em}}, \Psi)\sin\phi\,\mathrm{d}\phi, \\ \dfrac{\mathrm{d}\Psi}{\mathrm{d}t} = \dfrac{1}{2\pi}\displaystyle\int_0^{2\pi} -\frac{1}{A_{\mathrm{em}}\omega}\Gamma(A_{\mathrm{em}}, \Psi)\cos\phi\,\mathrm{d}\phi. \end{cases} \tag{30}$$

Therefore, equation (28) can be obtained as

$$\begin{aligned} \frac{\mathrm{d}A_{\mathrm{em}}}{\mathrm{d}t} &= -\frac{1}{2}(\xi + V_{\mathrm{em}})A_{\mathrm{em}} - \frac{1}{2\omega}f\sin(\Psi) \\ &= \frac{1}{2\omega}\left[\Xi_{\mathrm{em1}}(A_{\mathrm{em}}, \omega) - f\sin(\Psi)\right], \\ \frac{\mathrm{d}\Psi}{\mathrm{d}t} &= \frac{1}{128A_{\mathrm{em}}\omega}\Big[35\Omega_4 A_{\mathrm{em}}^7 + 40\Omega_3 A_{\mathrm{em}}^5 + 48\Omega_2 A_{\mathrm{em}}^3 \\ &\quad + 64\left(W_{\mathrm{em}} + \Omega_1 - \omega^2\right)A_{\mathrm{em}}\Big] - \frac{1}{2A_{\mathrm{em}}\omega}f\cos(\Psi) \\ &= \frac{1}{2A_{\mathrm{em}}\omega}\left[\Xi_{\mathrm{em2}}(A_{\mathrm{em}}, \omega) - f\cos(\Psi)\right]. \end{aligned} \tag{31}$$

Because the amplitude A_{em} and phase Ψ change slowly, $\mathrm{d}A_{\mathrm{em}}/\mathrm{d}t$ and $\mathrm{d}\Psi/\mathrm{d}t$ tend to and equation (31) is written as

$$\begin{aligned} &-\frac{1}{2}(\xi + V_{\mathrm{em}})A_{\mathrm{em}} - \frac{1}{2\omega}f\sin(\Psi) \\ &= \frac{1}{2\omega}\left[\Xi_{\mathrm{em1}}(A_{\mathrm{em}}, \omega) - f\sin(\Psi)\right] = 0, \\ &\frac{1}{128A_{\mathrm{em}}\omega}\Big[35\Omega_4 A_{\mathrm{em}}^7 + 40\Omega_3 A_{\mathrm{em}}^5 + 48\Omega_2 A_{\mathrm{em}}^3 \\ &+ 64\left(W_{\mathrm{em}} + \Omega_1 - \omega^2\right)A_{\mathrm{em}}\Big] - \frac{1}{2A_{\mathrm{em}}\omega}f\cos(\Psi) \\ &= \frac{1}{2A_{\mathrm{em}}\omega}\left[\Xi_{\mathrm{em2}}(A_{\mathrm{em}}, \omega) - f\cos(\Psi)\right] = 0. \end{aligned} \tag{32}$$

Because $\sin^2\Psi + \cos^2\Psi = 1$, the average amplitude–frequency of the Eq. (32) response can be expressed as follows:

$$W(A_{\mathrm{em}}, \omega) = \Xi_{\mathrm{em1}}(A_{\mathrm{em}}, \omega)^2 + \Xi_{\mathrm{em2}}(A_{\mathrm{em}}, \omega)^2 - f^2 = 0. \tag{33}$$

When the MLSM has QZS characteristics, by letting $a = \sqrt{2}/2$, $b = 1$, $c = 1/2$, $d = 1/2$, $\alpha = 4$, and $\beta = 2$, equation (26) can be expressed as

$$P(y) = W_{\mathrm{em}} y + \frac{3y^3}{2} - \frac{3y^5}{8} + \frac{39y^7}{16}. \tag{34}$$

The average amplitude–frequency response is given by

$$\begin{aligned} W(A_{\mathrm{em}}, \omega) &= \Xi_{\mathrm{em1QZS}}(A_{\mathrm{em}}, \omega)^2 + \Xi_{\mathrm{em2QZS}}(A_{\mathrm{em}}, \omega)^2 - f^2 \\ &= 0, \end{aligned} \tag{35}$$

where

$$\begin{cases} \Xi_{\mathrm{em1QZS}}(A_{\mathrm{em}}, \omega) = \Xi_{\mathrm{em1}}(A_{\mathrm{em}}, \omega) = -(\xi + V_{\mathrm{em}})\omega A_{\mathrm{em}}, \\ \Xi_{\mathrm{em2QZS}}(A_{\mathrm{em}}, \omega) = \left(W_{\mathrm{em}} - \omega^2\right)A_{\mathrm{em}} + \dfrac{9}{8}A_{\mathrm{em}}^3 \\ \qquad\qquad - \dfrac{15}{64}A_{\mathrm{em}}^5 + \dfrac{1365}{1024}A_{\mathrm{em}}^7. \end{cases}$$

Figure 5 shows the amplitude–frequency response curves of the MLSM with different excitation amplitudes f, electromechanical coupling coefficients η, electromagnetic coupling coefficients γ and ratios of resistance to inductance constant λ. The parameters are shown as follows: $a = \sqrt{2}/2$, $b = 1$, $c = 1/2$, $d = 1/2$, $\alpha = 4$, $\beta = 2$, $\omega = 1$, $\xi = 0.1$, and (a) $\eta = 0.05$, $\gamma = 0.4$, $\lambda = 0.6$, (b) $f = 0.01$, $\gamma = 0.4$, $\lambda = 0.6$, (c) $f = 0.01$, $\eta = 0.05$, $\lambda = 0.6$, (d) $f = 0.01$, $\eta = 0.05$, $\gamma = 0.4$. When the frequency ω increases, the amplitude increases to the resonance peak and then decreases, which corresponds to the typical nonlinear hard characteristic. As shown in Fig. 5(a), when f increases, the value of the resonance peak increases and the frequency ω corresponding to the resonance peak increases at the same time. The unstable solution region has been marked in Fig. 5(a); when the external disturbance appears in this region the solution will jump to the other corresponding solutions. The green zone in Fig. 5(a) is the multisolution region of the amplitude–frequency response curves when $f = 0.01$. In Figs. 5(b) and 5(c), when η and γ increase, the value of the resonance peak decreases but the frequency ω corresponding to the value of the resonance peak increases. When the frequency is high enough, η and γ

have little effect on the amplitude–frequency response curve of the MLSM. As shown in Fig. 5(d), when λ changes, the amplitude–frequency response curve hardly changes. Overall, the amplitude–frequency response curves have hard characteristics, showing the same result as in Fig. 3(a).

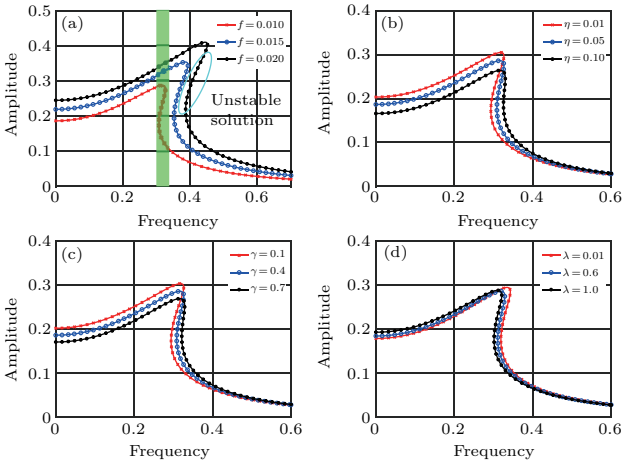


Fig. 5. The influence of different (a) excitation amplitudes and (b)–(d) electromechanical coefficients on the amplitude–frequency response curves of the MLSM.

3.2. Force transmissibility analysis of QZS system

To analyze the vibration isolation performance of the MLSM, this subsection analyzes the effects of different parameters on the force transmissibility. The definition of the force transmissibility T_y is

$$T_y = \frac{F_y(y)}{f}, \tag{36}$$

where $F_y(y)$ is the force transmitted to the base, which can be deduced as

$$F_y(y) = (\xi + V_{\mathrm{em}})\dot{y} + P_{\mathrm{E}}(y). \tag{37}$$

When the MLSM has QZS characteristics, we take the parameters $a=\sqrt{2}/2$, $b=1$, $c=1/2$, $d=1/2$, $\alpha=4$, and $\beta=2$, and the amplitude of $F_y(y)$ can be expressed in the form of decibels

$$F_{y1}(A_{\mathrm{em}}) = \sqrt{\Xi_{\mathrm{em1QZS}}(A_{\mathrm{em}},\omega)^2 + \Xi_{\mathrm{em2QZS}}(A_{\mathrm{em}},\omega)^2}. \tag{38}$$

Therefore, the force transmissibility of the MLSM with QZS characteristics is given by

$$T_{y1} = \frac{\sqrt{\Xi_{\mathrm{em1QZS}}(A_{\mathrm{em}},\omega)^2 + \Xi_{\mathrm{em2QZS}}(A_{\mathrm{em}},\omega)^2}}{f}. \tag{39}$$

Figure 6 describes the force transmissibility–frequency curves of a MLSM with different excitation amplitudes f, electromechanical coupling coefficients η, electromagnetic coupling coefficients γ and ratios of resistance λ to inductance constant. The parameters are as follows: $a=\sqrt{2}/2$, $b=1$, $c=1/2$, $d=1/2$, $\alpha=4$, $\beta=2\omega=1$, $\xi=0.1$ and (a) $\gamma=0.4$, $\lambda=0.6$, $\eta=0.05$, (b) $f=0.01$, $\gamma=0.4$, $\lambda=0.6$, (c) $f=0.01$, $\lambda=0.6$, $\eta=0.05$, (d) $f=0.01$, $\gamma=0.4$, $\eta=0.05$. As the external excitation frequency ω increases, the force transmissibility T_{y1} increases and then decreases rapidly, but the force transmissibility hardly changes when the external excitation frequency is large enough. As shown in Fig. 6(a), when f increases, the maximum value of the force transmissibility T_{y1} increases, as does the frequency ω corresponding to the maximum value. When the frequency ω is low, the force transmissibility decreases with increase in f. On the contrary, the force transmissibility increases with increases in f when the frequency ω is high enough. In Figs. 6(b) and 6(c), when η and γ increase the maximum value of the force transmissibility T_y gradually decreases, and the frequency corresponding to the maximum value increases at the same time. The force transmissibility curves gradually decrease with increase in η and γ when the frequency is low and increase during the high-frequency stage. It can be seen from Fig. 6(d) that when λ increases, the maximum value of the force transmissibility T_{y1} gradually decreases. Meanwhile, the frequency ω corresponding to the maximum value increases, and the force transmissibility T_{y1} curve is almost unchanged during the low-frequency stage and gradually increases when the frequency is high.

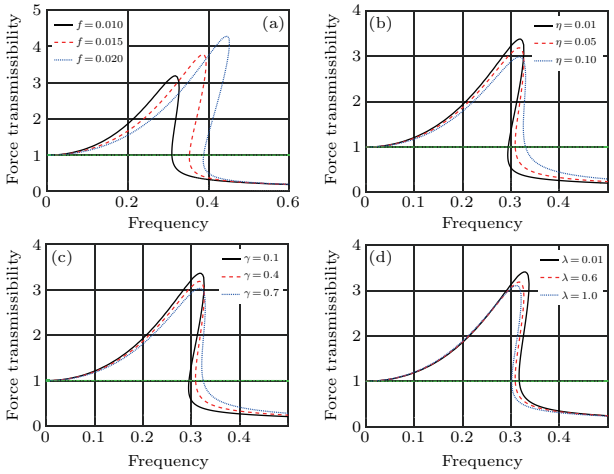


Fig. 6. The influence of different (a) excitation amplitudes and (b)–(d) electromechanical coefficients on the force transmissibility-frequency curves of the MLSM.

3.3. Energy harvesting performance of a QZS system

To study the energy harvesting performance of the MLSM, this subsection analyzes the harvested power of the system. The harvested power can be obtained as $P(t) = I_{\mathrm{R}}^2(t)R$. By introducing the transformation $P_{\mathrm{R}}(t) = [(R_{\mathrm{d}} + R_{\mathrm{c}})B_{\mathrm{e}}L_{\mathrm{c}}P(t)]/mL_{\mathrm{i}}R$, the harvested power can be written as

$$P_{\mathrm{R}}(t) = \lambda\eta I_{\mathrm{R}}^2(t). \tag{40}$$

The term $\omega(A_{\mathrm{em}},\phi)\cos\phi(t) - \lambda\sin\phi(t)$ in Eq. (22) can be written as

$$\omega(A_{\mathrm{em}},\phi)\cos\phi(t) - \lambda\sin\phi(t)$$

$$= \sqrt{\lambda^2+\omega^2(A_{\rm em},\phi)} \times\cos\left[\phi(t)+\arctan\left(\frac{\lambda}{\omega(A_{\rm em},\phi)}\right)\right]. \quad (41)$$

Then the amplitude of the output current $I_{\rm R}(t)$ is

$$I_{\rm R}(t) = \frac{\gamma\omega(A_{\rm em},\phi)}{\sqrt{\lambda^2+\omega^2(A_{\rm em},\phi)}}A_{\rm em}(t) \times\cos\left[\phi(t)+\arctan\left(\frac{\lambda}{\omega(A_{\rm em},\phi)}\right)\right]. \quad (42)$$

Therefore, the harvested power of the system $E_{\rm st}[P_{\rm R}]$ can be deduced as

$$E_{\rm st}[P_{\rm R}] = \lambda\eta E_{\rm st}\left[I_{\rm R}^2\right] = \lambda\eta\frac{\gamma^2\omega^2(A_{\rm em},\phi)}{\lambda^2+\omega^2(A_{\rm em},\phi)}E_{\rm st}\left[A_{\rm em}^2\right]. \quad (43)$$

To analyze the harvested power of the QZS system, let the parameters $a=\sqrt{2}/2$, $b=1$, $c=1/2$, $d=1/2$, $\alpha=4$, and $\beta=2$, and the harvested power $E_{\rm stQZS}[P_{\rm R}]$ can be expressed as

$$E_{\rm stQZS}[P_{\rm R}] = \lambda\eta\frac{\gamma^2\omega^2(A_{\rm em},\phi)}{\lambda^2+\omega^2(A_{\rm em},\phi)}\overline{A_{\rm emQZS}}^2, \quad (44)$$

where $\overline{A_{\rm emQZS}}$ is the average amplitude of a QZS system with EMT, which is given by Eq. (36).

Figure 7 describes the harvested power–frequency curves of the MLSM with different excitation amplitudes f, electromechanical coupling coefficients η, electromagnetic coupling coefficients γ and ratios of resistance to inductance constant λ. The parameters are $a=\sqrt{2}/2$, $b=1$, $c=1/2$, $d=1/2$, $\alpha=4$, $\beta=2$, $\omega=1$, $\xi=0.1$, and (a) $\gamma=0.4$, $\lambda=0.6$, $\eta=0.05$, (b) $f=0.01$, $\gamma=0.4$, $\lambda=0.6$, (c) $f=0.01$, $\lambda=0.6$, $\eta=0.05$, (d) $f=0.01$, $\gamma=0.4$, $\eta=0.05$. In Figs. 7(a)–7(c), when f, η, and γ increase, the harvested power $E_{\rm stQZS}[P_{\rm R}]$ gradually increases, and the frequency ω corresponding to the maximum value of the harvested power increases at the same time. This phenomenon means that f, η, γ, and λ have a positive effect on the harvested power. As shown in Fig. 7(d), when λ increases, the maximum value of the harvested power $E_{\rm stQZS}[P_{\rm R}]$ increases and then decreases.

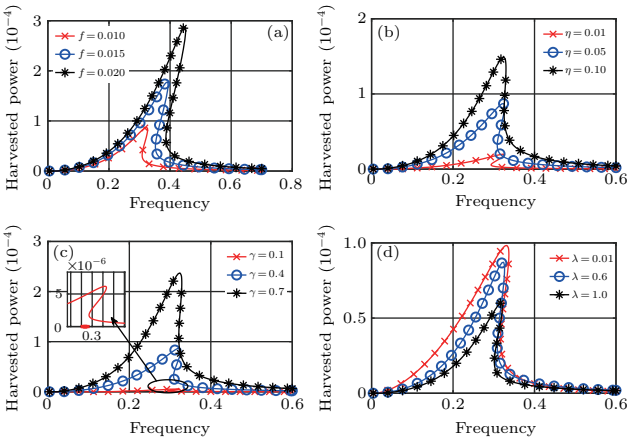


Fig. 7. The influence of different (a) excitation amplitudes and (b)–(d) electromechanical coefficients on the harvested power-frequency curves of the MLSM.

4. Energy harvesting under random excitation

To study the energy harvesting performance of the QZS system with EMT under random excitation, Gaussian white noise is selected as the external excitation of the system. Gaussian white noise can be written as $\hat{y}=-\varsigma(t)$, and the average value of $\varsigma(t)$ is 0. Meanwhile, $\varsigma(t)$ satisfies $\langle\varsigma(t)\varsigma(t')=2\sigma\delta(t-t')\rangle$, where $\langle\cdots\rangle$ represents averaging with respect to $\varsigma(t)$. σ is the noise intensity and δ is the Dirac delta equation.

4.1. Comparative analysis of QZS and a quad-stable system

Equation (24) can be written as

$$\begin{cases}\dfrac{{\rm d}y}{{\rm d}t}=v,\\ \dfrac{{\rm d}v}{{\rm d}t}=-(\xi+V_{\rm em})v-P(y)+\varsigma(t),\end{cases} \quad (45)$$

where

$$P(y) = (W_{\rm em}+\beta)y - y\left(-1+\frac{c}{\sqrt{b^2-y^2}}\right) \times\left(1-\frac{d}{\sqrt{a^2-\left(c-\sqrt{b^2-y^2}\right)^2}}\right) -\alpha y\left(1-\frac{c}{\sqrt{b^2-y^2}}\right). \quad (46)$$

The Fokker–Planck–Kolmogorov equation for the probability density function corresponding to the displacement y and velocity v of Eq. (46) is given by

$$\frac{\partial}{\partial t}p = -\frac{\partial}{\partial y}zp-\frac{\partial}{\partial v}\left[-(\xi+V_{\rm em})v\right]p -\frac{\partial}{\partial v}\left[-P(y)\right]p+\frac{\partial^2}{\partial v^2}p, \quad (47)$$

where $p=p(y,v,t)$ is the transition probability density function of the displacement y and velocity v.

The $p_{\rm st}(y,v)$ is the distribution of stationary displacement y and velocity v, which can be obtained as

$$p_{\rm st}(y,v)=N_1{\rm e}^{[-U_{\rm eff}(y,v)]}, \quad (48)$$

where N_1 is a normalized constant, and the effective potential energy $U_{\rm eff}(y,v)$ can be expressed as

$$U_{\rm eff}(y,v)=\frac{1}{\sigma}(\xi+V_{\rm em})U_1, \quad (49)$$

$$U_1=\frac{1}{2}v^2+\frac{1}{2}W_{\rm em}y^2 +\left(\frac{1}{2}y^2+c\sqrt{b^2-y^2}-d\sqrt{a^2-\left(c-\sqrt{b^2-y^2}\right)^2}\right)$$

$$+\frac{\alpha}{2}\left(c-\sqrt{b^2-y^2}\right)^2+\frac{\beta}{2}y^2. \tag{50}$$

The mean squares of displacement y and velocity v are $E_{\rm st}\left[y^2\right]$ and $E_{\rm st}\left[v^2\right]$, respectively, which can be written as

$$\begin{cases} E_{\rm st}\left[y^2\right]=\displaystyle\int_{-\infty}^{+\infty}\int_{-\infty}^{+\infty}y^2 p_{\rm st}\left(y,v\right)\mathrm{d}y\mathrm{d}v, \\ E_{\rm st}\left[v^2\right]=\displaystyle\int_{-\infty}^{+\infty}\int_{-\infty}^{+\infty}v^2 p_{\rm st}\left(y,v\right)\mathrm{d}y\mathrm{d}v. \end{cases} \tag{51}$$

Let $A_{\rm em}=\sqrt{y^2+v^2}$, the mean of the harvested power $E_{\rm st}\left[P_{\rm R}\right]$ can be deduced as

$$E_{\rm st}\left[P_{\rm R}\right]=\lambda\eta\frac{\gamma^2\omega^2\left(A_{\rm em},\phi\right)}{\lambda^2+\omega^2\left(A_{\rm em},\phi\right)}E_{\rm st}\left[y^2+v^2\right]. \tag{52}$$

The effective potential energy, probability density of displacement, mean square value of displacement and harvested power of the quad-stable characteristic and QZS characteristic of the MLSM are shown in Fig. 8. The parameters are $\omega=1$, $\sigma=0.001$, $\xi=0.1$, $\gamma=0.4$, $\lambda=0.6$, and $\eta=0.01$. The geometric coefficients and natural frequency ratios are $a=\sqrt{2}/2$, $b=1$, $c=1/2$, $d=1/2$, $\alpha=4$, and $\beta=2$ for QZS characteristics and $a=3/5$, $b=1$, $c=3/5$, $d=1/2$, $\alpha=1/50$, and $\beta=1/50$ for quad-stable characteristics. As shown in Fig. 8(a), the MLSM with quad-stable characteristics has a wider potential well than the QZS one. It can be seen from Fig. 8(b) that the probability density of displacement of the MLSM with quad-stable characteristics is distributed within a larger displacement range. In Figs. 8(c) and 8(d), as the noise intensity σ increases, the mean square value of displacement and the harvested power increase. Moreover, compared with the MLSM with QZS characteristics, the energy harvesting performance of the MLSM with quad-stable characteristics is more obvious. That is because the MLSM with quad-stable characteristic has a wider potential well than the QZS one.

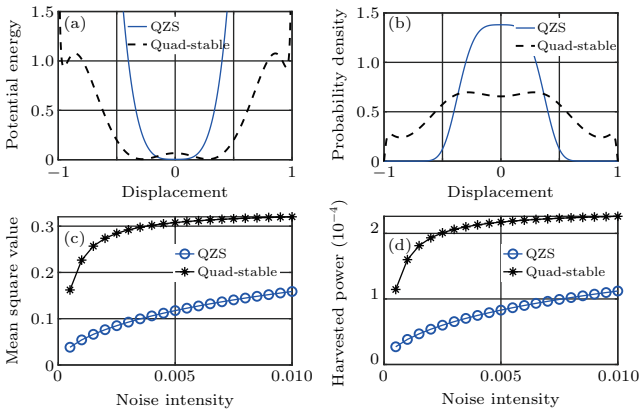


Fig. 8. Comparative analyses of (a) effective potential energy, (b) probability density of displacement, (c) mean square value of displacement and (d) harvested power of the MLSM with QZS and quad-stable characteristics.

4.2. Energy harvesting performance of a QZS system

Figures 9 and 10 describe the mean square value of displacement–noise intensity and harvested power–noise intensity curves with different electromechanical coupling coefficients η, electromagnetic coupling coefficients γ and ratios of resistance to inductance constant λ. The parameters are $a=\sqrt{2}/2$, $b=1$, $c=1/2$, $d=1/2$, $\alpha=4$, $\beta=2$, $\xi=0.1$, and (a) $\gamma=0.4$, $\lambda=0.6$, (b) $\lambda=0.6$, $\eta=0.05$, (c) $\gamma=0.4$, $\eta=0.05$. As shown in Figs. 9(a)–9(b), with a gradual increase in η and γ, the mean square value of the displacement gradually decreases, while the influence of λ on the mean square value of the displacement is not obvious, as can be seen in Fig. 9(c). In Figs. 10(a)–10(c), when the parameters η, γ, and λ increase, the average harvested power gradually increases. Therefore, the parameters η, γ, and λ have a positive effect on the energy harvesting performance of the QZS system under random excitation.

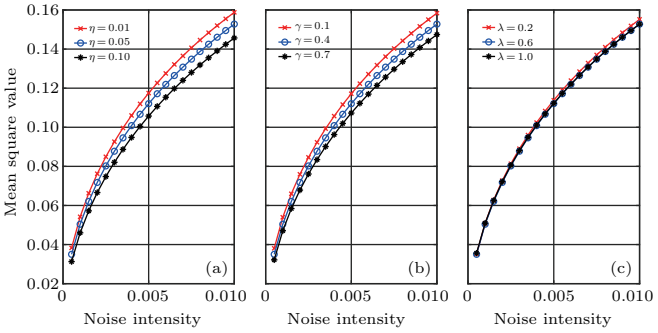


Fig. 9. The influence of different (a) electromechanical coupling coefficients η, (b) electromagnetic coupling coefficients γ and (c) ratios of resistance λ to inductance constant on mean square value of displacement.

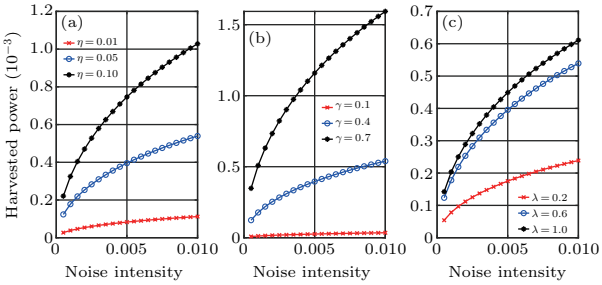


Fig. 10. The influence of different (a) electromechanical coupling coefficients η, (b) electromagnetic coupling coefficients γ and (c) ratios of resistance to inductance constant λ on harvested power.

5. Performance comparisons for different cases

This section compares two different models, case I and case Ⅱ, with the MLSM to explore the VIEH performance. Case I corresponds to a MLSM without vertical linear spring Ⅱ and rigid link I ($a=0$ and $k_1=0$) while case Ⅱ corresponds to a MLSM without a horizontal linear spring ($k_2=0$), as can be seen in Fig. 11. For easy comparison, let the geometric coefficients and natural frequency ratios of the MLSM be $a=\sqrt{5}/4$, $b=1$, $c=3/4$, $d=\alpha=1$, $\beta=1/4$, for case I $b=1$, $c=3/4$,

$\rho = 1/4$ and for case Ⅱ $a = \sqrt{5}/4$, $b = 1$, $c = 3/4$, $d = 1$, $1/4$. For more information, see Appendices A and B.

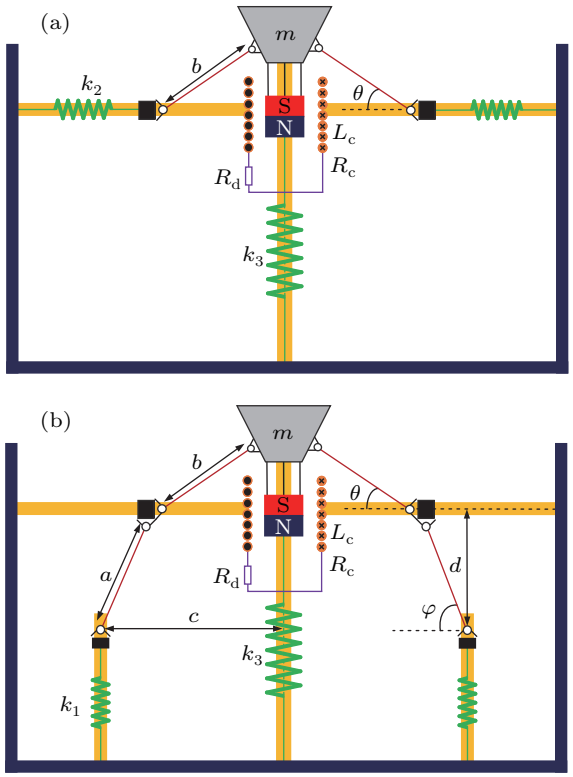


Fig. 11. Two different types of QZS oscillator: (a) case I and (b) case Ⅱ.

5.1. Comparative analysis of vibration isolation performance of a QZS system

Figure 12 compares the curves of the amplitude–frequency response of case I and case Ⅱ with the MLSM. The parameters are as follows: $f = 0.01$, $\xi = 0.1$, $\gamma = 0.4$, $\lambda = 0.6$, $\eta = 0.05$. The results show that when the EMT is taken into account, the resonance peak of the three models reduces and moves into the low-frequency region. Case I has the largest resonance peak and case Ⅱ has the smallest one. When the frequency ω is low, the value of the amplitude decreases as case I, the MLSM and case Ⅱ. On the contrary, the amplitude of case I, the MLSM and case Ⅱ decrease sequentially when the frequency ω is high. This is due to the fact that when the EMT is taken into account, it is equivalent to adding damping $(\eta\gamma\lambda)/\left[\lambda^2+\omega^2(A_{\mathrm{em}},\phi)\right]$ and stiffness $\left[\eta\gamma\omega^2(A_{\mathrm{em}},\phi)\right]/\left[\lambda^2+\omega^2(A_{\mathrm{em}},\phi)\right]$ to the isolators. The peak value decreases because of damping, and when the stiffness increases the natural frequency will become larger and the resonance peak will move to the high-frequency region.

Figure 13 compares the stiffness–displacement curves for cases I and Ⅱ with the MLSM under QZS characteristics. The vibration isolation bandwidth of the MLSM is slightly smaller than that of cases I and Ⅱ, and the vibration isolation bandwidth of cases I and Ⅱ is basically the same.

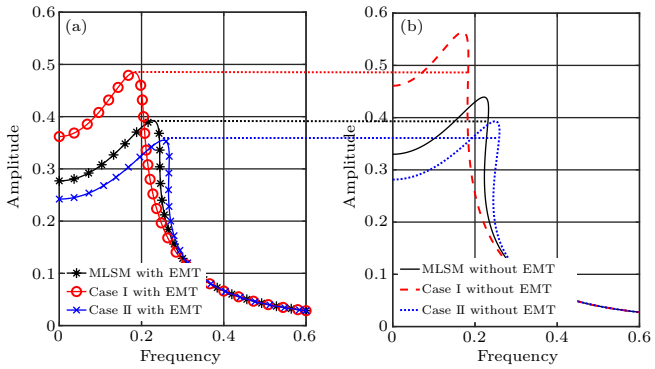


Fig. 12. The amplitude-frequency response curves of the MLSM for cases I and Ⅱ.

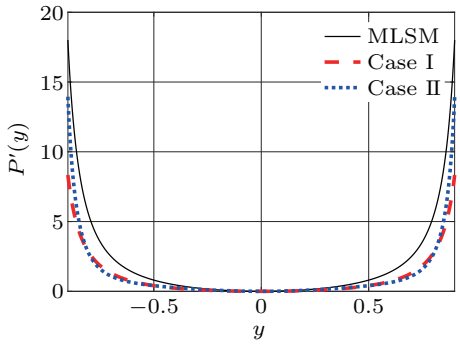


Fig. 13. The stiffness curves for the MLSM, case I and case Ⅱ.

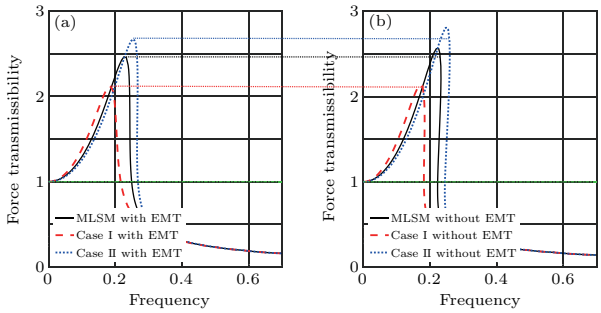


Fig. 14. The force transmissibility–frequency curves of the MLSM, case I and case Ⅱ. The parameters are $f = 0.01$, $\xi = 0.1$, $\gamma = 0.4$, $\lambda = 0.6$ and $\eta = 0.05$.

Figure 14 compares the force transmissibility–frequency response curves of cases I and Ⅱ and the MLSM. The parameters are as follows: $f = 0.01$, $\xi = 0.1$, $\gamma = 0.4$, $\lambda = 0.6$, $\eta = 0.05$. The results show that when EMT is considered, the maximum value of the force transmissibility of the three isolators reduces, and the maximum value moves to the direction of high frequency. This is because the EMT increases the damping ratio and natural frequency of the isolators. In a word, the parameters η, γ, and λ have a positive effect on the vibration isolation effect. Case Ⅱ has the largest maximum value of force transmissibility and case I the smallest. The frequency ω corresponding to the maximum force transmissibility of case Ⅱ is the largest while case I has the smallest one. When the frequency ω is low, the force transmissibility of the three isolators is basically the same. When the frequency ω is high, the force transmissibility of case Ⅱ, the MLSM and case I

decreases sequentially. Therefore, of the three isolators, case I has the best vibration isolation, followed by the MLSM; case Ⅱ is the worst. This result corresponds to Figs. 12 and 13.

5.2. Comparative analysis of energy harvesting performance of a QZS system

Figure 15 compares the harvested power–frequency curves of cases I and Ⅱ with the MLSM under harmonic excitation. The parameters are as follows: $f = 0.01$, $\xi = 0.1$, $\gamma = 0.4$, $\lambda = 0.6$, $\eta = 0.05$. The results show that the maximum value of the harvested power of case I is the largest, and the frequency ω corresponding to the maximum value is the lowest compared with the other two isolators (the MLSM and case Ⅱ). In contrast, the maximum value of the harvested power of case Ⅱ is the smallest, and the frequency ω corresponding to the maximum value is the highest. In the low-frequency region, the value of harvested power of case I, the MLSM and case Ⅱ decreases sequentially. On the contrary, the harvested power decrease follows as case Ⅱ, the MLSM and case I when the frequency ω is high. Thus, case I has the best energy harvesting effect, followed by the MLSM; case Ⅱ is the worst.

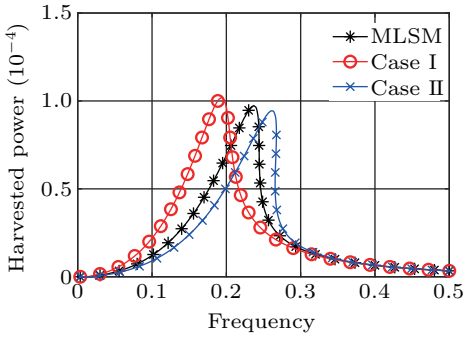


Fig. 15. Comparative analysis of harvested power–frequency response curves of the MLSM, case I and case Ⅱ.

Figure 16 describes the effective potential energy, probability density of displacement, mean square value of displacement and harvested power of cases I and Ⅱ and the MLSM under random excitation. All three isolators have QZS characteristics. In Fig. 16(a), the potential well of the case I system is narrower than that of the MLSM and case Ⅱ. As shown in Fig. 16(b), the probability density of displacement of the case I system is narrower than for the MLSM and case Ⅱ. Figures 16(c)–16(d) show the change in the mean square value of displacement and the mean square value of harvested power with noise intensity σ. It can be seen from Figs. 16(c)–16(d), that as the noise intensity σ increases, the probability density of displacement and harvested power increase. Compared with case I, the low-frequency power harvesting performances of the MLSM and case Ⅱ are more obvious. As shown in Figs. 16(a)–16(d), the potential well width, probability density of displacement width and low-frequency power harvesting performance of the MLSM is basically the same as that of case Ⅱ.

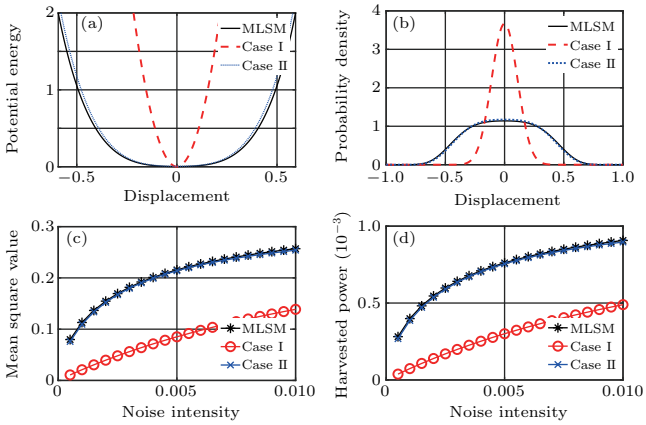


Fig. 16. Comparative analysis of (a) effective potential energy, (b) probability density of displacement, (c) mean square value of displacement and (d) harvested power of the MLSM, case I and case Ⅱ. The parameters are $\sigma = 0.001$, $\xi = 0.1$, $\gamma = 0.4$, $\lambda = 0.6$, $\eta = 0.05$.

5.3. Comparative analysis of energy harvesting performance of a multistable system

Figure 17 shows the effective potential energy, probability density of displacement, mean square value of displacement and harvested power of cases I and Ⅱ and the MLSM under random excitation. The parameters are $\sigma = 0.001$, $\xi = 0.1$, $\gamma = 0.4$, $\lambda = 0.6$, $\eta = 0.05$. And the geometric coefficients and natural frequency ratios are as follows: $a = 3/5$, $b = 1$, $c = 3/5$, $d = 1/2$, $\alpha = 1/20$, $\beta = 1/100$ for the MLSM, $b = 1$, $c = 1/4$, $\rho = 1/5$ for case I and $a = 3/5$, $b = 1$, $c = 7/10$, $d = 7/10$, $\beta = 1/100$ for case Ⅱ. All three isolators have multistable potential well characteristics. As shown in Fig. 17(a), the MLSM has a wider potential well than cases I and Ⅱ. It can be seen from Fig. 17(b) that the probability density of displacement of the MLSM is distributed within a wider displacement range. That is because the MLSM has quad-stable potential well characteristics and the other two isolators (cases I and Ⅱ) only have bistable ones. In Figs. 17(c)–17(d), as the noise intensity σ increases, the mean square value of displacement and harvested power of the three models increase. Moreover, compared with the other two models, the energy harvesting performance of the MLSM is more obvious. In the ultra-

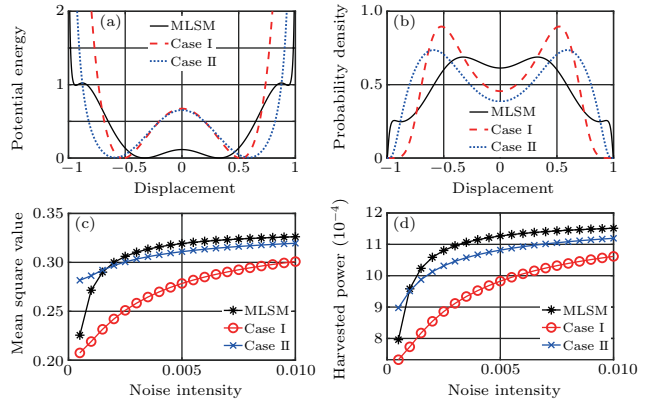


Fig. 17. Comparative analysis of (a) effective potential energy, (b) probability density of displacement, (c) mean square value of displacement and (d) harvested power for the MLSM, case I and case Ⅱ.

low frequency region, the probability density of displacement and mean square value of harvested power of the MLSM are lower than for case I. That is because the external excitation is too low for the MLSM to achieve interwell oscillation.

6. Conclusion

To achieve VIEH performance at low frequencies, this paper proposes a MLSM. By using Newton's law and Kirchhoff's law, this paper derives a theoretical model. Through the analysis of the dimensionless stiffness near the equilibrium position, the QZS characteristic of the MLSM are found. At the same time, by adjusting the parameters, the MLSM can achieve multistable characteristic. The effects of different parameters on the VIEH performance of the MLSM with QZS characteristic under harmonic excitation are analyzed by using the averaging method. The results show that the MLSM can isolate vibration while harvesting vibration energy. Subsequently, this work uses the Fokker–Planck–Kolmogorov equation to analyze the energy harvesting performance of the MLSM under Gaussian white noise. The results show that a MLSM with multistable potential well characteristics has a better energy harvesting performance than with QZS characteristic. Finally, the MLSM and two other special cases based on QZS characteristic (cases I and Ⅱ) are compared: the vibration isolation performance of the MLSM and the other two cases is basically the same. However, due to its quadstable characteristic, the MLSM has a better energy harvesting performance. The performance of the MLSM proves that it can be widely used in vibration isolation and power supplies to structural health monitoring device.

Appendix A: Case I: QZS oscillator with EMT

According to Newton's law and Kirchhoff's law, the dimensionless uncoupled dynamic equation for case I can be expressed as

$$\begin{aligned}&\ddot{y}+(\xi+V_{\rm em})+(W_{\rm em}+\rho)\,y-y\left(1-\frac{c}{\sqrt{b^2-y^2}}\right)\\&=f\cos(\omega t),\quad |y|<b,\end{aligned}\tag{A1}$$

where $\rho=\omega_3^2/\omega_2^2$.

The dimensionless restoring force produced by the springs of case I can be deduced as

$$P_2(y)=\rho y-y\left(1-\frac{c}{\sqrt{b^2-y^2}}\right).\tag{A2}$$

The dimensionless stiffness of case I is given by

$$P_2'(y)=\frac{cy^2}{\left(b^2-y^2\right)^{3/2}}+\left(\frac{c}{\sqrt{b^2-y^2}}-1\right)+\rho.\tag{A3}$$

Only when $y=0$ and $B-1+\rho=0$ does case I have QZS characteristic.

We expand Eq. (A2) using the Taylor theorem

$$P_2(y)=(W_{\rm em}+\Omega_{21})\,y+\Omega_{22}y^3+\Omega_{23}y^5+\Omega_{24}y^7,\tag{A4}$$

where

$$\begin{cases}\Omega_{21}=\left(-1+\dfrac{c}{b}+\rho\right),\\ \Omega_{22}=\dfrac{c}{2b^3},\\ \Omega_{23}=\dfrac{3c}{8b^5},\\ \Omega_{24}=\dfrac{5c}{16b^7}.\end{cases}$$

Using the extended averaging method, the amplitude response–frequency response of case I can be written as

$$\begin{aligned}W_2(A_{\rm em},\omega)&=\Xi_{\rm em21}(A_{\rm em},\omega)^2+\Xi_{\rm em22}(A_{\rm em},\omega)^2-f^2\\&=0,\end{aligned}\tag{A5}$$

where

$$\begin{cases}\Xi_{\rm em22}(A_{\rm em},\omega)=(\xi+V_{\rm em})\,\omega A_{\rm em},\\ \Xi_{\rm em22}(A_{\rm em},\omega)=\left(W_{\rm em}+\Omega_{21}-\omega^2\right)A_{\rm em}+\dfrac{3}{4}\Omega_{22}A_{\rm em}^3\\ \qquad\qquad+\dfrac{5}{8}\Omega_{23}A_{\rm em}^5+\dfrac{35}{64}\Omega_{24}A_{\rm em}^7.\end{cases}$$

The force transmitted to the base can be expressed as

$$F_{y2}(y)=(\xi+V_{\rm em})+P_2(y)+W_{\rm em}y.\tag{A6}$$

The amplitude of the transmitted force for case I with QZS characteristics is given by

$$F_{y2}(A_{\rm em})=\sqrt{\Xi_{\rm em21}(A_{\rm em},\omega)^2+\Xi_{\rm em22}(A_{\rm em},\omega)^2}.\tag{A7}$$

Thus, the force transmissibility of case I is given by

$$T_{y2}=\frac{\sqrt{\Xi_{\rm em21}(A_{\rm em},\omega)^2+\Xi_{\rm em22}(A_{\rm em},\omega)^2}}{f}.\tag{A8}$$

The energy harvesting power $E_{\rm st2}[P_{\rm R}]$ of case I can be deduced as

$$E_{\rm st2}[P_{\rm R}]=\lambda\eta\frac{\gamma^2\omega^2(A_{\rm em},\phi)}{\lambda^2+\omega^2(A_{\rm em},\phi)}\overline{A_{\rm em2}}^2,\tag{A9}$$

where $\overline{A_{\rm em2}}$ is the average amplitude of case I, which can be given by Eq. (A5).

Appendix B: Case Ⅱ: QZS oscillator with EMT

According to Newton's law and Kirchhoff's law, the dimensionless uncoupled dynamic equation of case Ⅱ can be expressed as

$$\ddot{y}+(\xi+V_{\mathrm{em}})+(W_{\mathrm{em}}+\beta)y-y\left(-1+\frac{c}{\sqrt{b^2-y^2}}\right)\times\left(1-\frac{d}{\sqrt{a^2-\left(c-\sqrt{b^2-y^2}\right)^2}}\right)=f\cos(\omega t),\quad |y|<b. \tag{B1}$$

The dimensionless restoring force produced by the springs of case Ⅱ is given by

$$P_3(y)=\beta y-y\left(-1+\frac{c}{\sqrt{b^2-y^2}}\right)\times\left(1-\frac{d}{\sqrt{a^2-\left(c-\sqrt{b^2-y^2}\right)^2}}\right). \tag{B2}$$

The dimensionless stiffness of case Ⅱ can be deduced as

$$P_3'(y)=\frac{dy^2\left(c-\sqrt{b^2-y^2}\right)^2}{(b^2-y^2)\left(a^2-\left(c-\sqrt{b^2-y^2}\right)^2\right)^{3/2}}-\frac{cy^2\left(1-\frac{d}{\sqrt{a^2-\left(c-\sqrt{b^2-y^2}\right)^2}}\right)}{(b^2-y^2)^{3/2}}+\left(\frac{c}{\sqrt{b^2-y^2}}-1\right)\times\left(\frac{d}{\sqrt{a^2-\left(c-\sqrt{b^2-y^2}\right)^2}}-1\right)+\beta. \tag{B3}$$

Only when $y=0$ and $(B-1)\left(\frac{C}{\sqrt{A^2-(1-B)^2}}-1\right)+\beta=0$ does case Ⅱ have QZS characteristic.

We expand Eq. (B2) using the Taylor theorem

$$P_3(y)=(W_{\mathrm{em}}+\Omega_{31})y+\Omega_{32}y^3+\Omega_{33}y^5+\Omega_{34}y^7, \tag{B4}$$

where

$$\Omega_{31}=(1-\frac{c}{b})(1-\frac{d}{\sqrt{a^2-(b-c)^2}})+\beta,$$

$$\Omega_{32}=\frac{a^2c(-\sqrt{a^2-(b-c)^2}+d)+(b-c)^2(c(\sqrt{a^2-(b-c)^2}-d)+bd)}{2b^3\left(a^2-(b-c)^2\right)^{3/2}},$$

$$\Omega_{33}=\frac{1}{8}\left(-\frac{2(b-c)cd}{b^4\left(a^2-(b-c)^2\right)^{3/2}}+\frac{(b-c)\left(-3b^3-a^2c+7b^2c-5bc^2+c^3\right)d}{b^4\left(a^2-(b-c)^2\right)^{5/2}}+\frac{3c\left(\frac{d}{\sqrt{a^2-(b-c)^2}}-1\right)}{b^5}\right),$$

$$\Omega_{34}=\frac{5c\left(\frac{d}{\sqrt{a^2-(b-c)^2}}-1\right)}{16b^7}-\frac{3b(b-c)cd}{16b^7\left(a^2-(b-c)^2\right)^{3/2}}+\frac{c\left(3b^3+a^2c-7b^2c+5bc^2-c^3\right)d}{16b^6\left(a^2-(b-c)^2\right)^{5/2}}+\frac{(b-c)[5b^5-19b^4c+28b^3c^2+5b^2c(a^2-4c^2)-c\left(a^2-c^2\right)^2+b(-7a^2c^2+7c^4)]d}{16b^6\left(a^2-(b-c)^2\right)^{7/2}}.$$

Using the extended averaging method, the amplitude response–frequency response of case Ⅱ can be written as

$$W_3(A_{\mathrm{em}},\omega)=\Xi_{\mathrm{em31}}(A_{\mathrm{em}},\omega)^2+\Xi_{\mathrm{em32}}(A_{\mathrm{em}},\omega)^2-f^2=0, \tag{B5}$$

where

$$\begin{cases}\Xi_{\mathrm{em31}}(A_{\mathrm{em}},\omega)=(\xi+V_{\mathrm{em}})\omega A_{\mathrm{em}},\\ \Xi_{\mathrm{em32}}(A_{\mathrm{em}},\omega)=\left(W_{\mathrm{em}}+\Omega_{31}-\omega^2\right)A_{\mathrm{em}}+\frac{3}{4}\Omega_{32}A_{\mathrm{em}}^3+\frac{5}{8}\Omega_{33}A_{\mathrm{em}}^5+\frac{35}{64}\Omega_{34}A_{\mathrm{em}}^7.\end{cases}$$

The force transmitted to the base can be expressed as

$$F_{y3}(y)=(\xi+V_{\mathrm{em}})+P_3(y)+W_{\mathrm{em}}y. \tag{B6}$$

The amplitude of the transmitted force of case Ⅱ with QZS characteristics is given by

$$F_{y3}(A_{\mathrm{em}})=\sqrt{\Xi_{\mathrm{em31}}(A_{\mathrm{em}},\omega)^2+\Xi_{\mathrm{em32}}(A_{\mathrm{em}},\omega)^2}. \tag{B7}$$

Therefore, the force transmissibility of case Ⅱ is given by

$$T_{y3}=\frac{\sqrt{\Xi_{\mathrm{em31}}(A_{\mathrm{em}},\omega)^2+\Xi_{\mathrm{em32}}(A_{\mathrm{em}},\omega)^2}}{f}. \tag{B8}$$

The energy harvesting power $E_{\mathrm{st3}}[P_{\mathrm{R}}]$ of case Ⅲ can be deduced as

$$E_{\mathrm{st3}}[P_{\mathrm{R}}] = \lambda\eta\frac{\gamma^2\omega^2(A_{\mathrm{em}},\phi)}{\lambda^2+\omega^2(A_{\mathrm{em}},\phi)}\overline{A_{\mathrm{em3}}}^2, \tag{B9}$$

where $\overline{A_{\mathrm{em3}}}$ is the average amplitude of case Ⅲ, which can be given by Eq. (A5).

Acknowledgments

Project supported by Guangdong Basic and Applied Basic Research Foundation (Grant Nos. 2022A1515010967 and 2023A1515012821), the National Natural Science Foundation of China (Grant Nos. 12002272 and 12272293), and Opening Project of Applied Mechanics and Structure Safety Key Laboratory of Sichuan Province (Grant No. SZDKF-202101).

References

[1] Chai Y Y and Jing X J 2022 *Nonlinear Dyn.* **109** 2383
[2] Fulton F and Sorokin V S 2023 *Mech. Res. Commun.* **130** 104121
[3] Tian K Y, WangY L, CaoD Q and Yu K P 2023 *Int. J. Mech. Sci.* **265** 108902
[4] Ibrahim R A 2008 *J. Sound Vib.* **314** 371
[5] Liu Y Q, Ji W, Gu H S, Deng E J, Wang X and Song C F 2021 *J. Mech. Sci. Technol.* **35** 2313
[6] Yoshikazu A, Takehiko A, Kosuke K, Kosei M and Takeshi M 2013 *J. Sound Vib.* **332** 6063
[7] Yuan S J, Sun Y, Zhao J L, Meng K, Wang M, Pu H Y, Peng Y, Luo J and Xie S R 2020 *J. Sound Vib.* **482** 115449
[8] Georgios I F, Ioannis A A and Evangelos J S 2023 *Eng. Struct.* **291** 116389
[9] Zhang T, Shi P and Yue X K 2022 *Mech. Syst. Signal Process.* **179** 109351
[10] Sun X T and Jing X J 2015 *Mech. Syst. Signal Process.* **62–63** 149
[11] Yang T, Cao Q J and Hao Z F 2021 *Mech. Syst. Signal Process.* **155** 107636
[12] Yan G, Qi W H, Shi J W, Yan H, Zou H X, Zhao L C, Wu Z Y, Fang X Y, Li X Y and Zhang W M 2022 *J. Sound Vib.* **525** 116799
[13] Thomson A J and Thompson W A 1977 *Acta Biotheor* **26** 19
[14] Mehran S, Vladislav S, Brian M and Sinniah I 2022 *J. Sound Vib.* **526** 116822
[15] Yu C Y, Fu Q D, Zhang J R and Zhang N 2022 *Mech. Syst. Signal Process.* **180** 109378
[16] Gatti G, Brennan M J and Tang B 2019 *Mech. Syst. Signal Process.* **125** 4
[17] Orrego S, Shoele S, Ruas A, Doran K, Caggiano B, Mittal R and Kang S H 2017 *Appl. Energy* **194** 212
[18] Collins I, Hossain M, Dettmer W and Masters I 2021 *Renew. Sust. Energ. Rev.* **151** 111478
[19] Bai S M, Cui J, Zheng Y Q, Li G, Liu T S, Liu Y B, Hao C C and Xue C Y 2023 *Appl. Energy* **329** 120292
[20] Chen J E, Zhang W, Yao M H, Liu J and Sun M 2020 *Int. J. Nonlinear Sci. Numer.* **21** 1
[21] Liu Q, Qin W Y, Yang Y F and Zhou S X 2022 *Mech. Syst. Signal Process.* **178** 109291
[22] Drezet C, Kacem N and Bouhaddi N 2018 *Sens. Actuator A Phys.* **283** 54
[23] Jiang W A and Chen L Q 2016 *Int. J. Non-Linear Mech.* **85** 174
[24] Yang K, Fei F, An H C 2019 *Nonlinear Dyn.* **96** 2369
[25] Radeef Z 2023 *Open Eng.* **13** 20220409
[26] Yang T, Zhang Y Q, Zhou S X, Fan H W and Zhang X H 2022 *Commun. Nonlinear Sci. Numer. Simul.* **111** 106465
[27] Manh N V, Linh N N, Nguyen A T and Anh N D 2023 *Mech. Res. Commun.* **131** 104157
[28] Liu H F, Dong W W, Chang Y L, Gao Y F and Li W C 2022 *Rev. Sci. Instrum.* **93** 055001
[29] Zang J, Cao R Q, Zhang Y W, Fang B and Chen L Q 2021 *Commun. Nonlinear Sci. Numer. Simul.* **95** 105620
[30] Yang Y K and Yang B T 2021 *Int. J. Mech. Sci.* **199** 106411
[31] Wang K, Zhou J X, Ouyang H J, Chang Y P and Xu D L 2021 *Mech. Syst. Signal Process.* **151** 107368
[32] Huang B, Wang P Z, Wang L, Yang S and Wu D Z 2020 *Nanotechnol. Rev.* **9** 716
[33] Jin Y Z, Liu K F, Xiong L Y and Tang L H 2022 *Mech. Syst. Signal Process.* **181** 109479
[34] Yang T, Zhang Y Q, Zhou S X, Fan H W and Zhang X H 2022 *Commun. Nonlinear Sci. Numer. Simul.* **111** 106465
[35] Zhang Y Q, Yang T, Du H F and Zhou S X 2023 *Mech. Syst. Signal Process.* **184** 109689
[36] Tan D G, Zhou J X, Wang K, Zhao X H, Wang Q and Xu D L 2022 *Nano Energy* **92** 106746
[37] Huang X B and Yang B T 2021 *Mech. Syst. Signal Process.* **158** 107797
[38] Luo H C, Liu J Y, Yang T, Zhang Y Q and Cao Q J 2022 *Nano Energy* **103** 107755
[39] Yang X, Wang C and Lai S K 2020 *Eng. Struct.* **221** 110789
[40] Lai S K, Wang C and Zhang L H 2019 *Mech. Syst. Signal Process.* **122** 87
[41] Zhou S X, Lallart M and Erturk A 2022 *J. Sound Vib.* **528** 116886
[42] Yang T, Xu H T, Tang J and Zhou S X 2023 *Appl. Math. Model.* **119** 736
[43] Daqaq M F 2012 *Nonlinear Dyn.* **69** 1063
[44] Yang T, Zhou S X, Litak G and Jing X J 2023 *Nonlinear Dyn.* **111** 20525
[45] Yang T, Zhang Y Q and Zhou S X 2022 *Sci. China Technol. Sci.* **65** 631
[46] Lu Z Q, Wu D, Ding H and Chen L Q 2021 *Appl. Math. Model.* **89** 249
[47] Zou D L, Liu G Y, Rao Z S, Tan T, Zhang W M and Liao W H 2021 *Mech. Syst. Signal Process.* **147** 107101
[48] Liu C R, Zhao R, Yu K P, Lee H P and Liao B P 2021 *Energy* **233** 121146
[49] Zang J, Cao R Q, Fang B and Zhang Y W 2020 *J. Sound Vib.* **484** 115534
[50] Yang T, Zhou S X, Fang S T, Qin W Y and Inman D J 2021 *Appl. Phys. Rev.* **8** 031317
[51] Jiang W A and Chen L Q 2016 *Int. J. Non-Linear Mech.* **85** 174